Effects of Na deficiency on spin dynamics in the Mott insulating $Na_{4-x}Ir_3O_8$

Y. S. Choi,[1,*] C. H. Lee,[2,*] T. Kihara,[3,4] H. Zheng,[5] H. Nojiri,[3,†] J. F. Mitchell,[5,‡] and Kwang-Yong Choi[1,§]

[1]*Department of Physics, Sungkyunkwan University, Suwon, Gyeonggi-do 16419, Republic of Korea*

[2]*Department of Physics, Chung-Ang University, Seoul 06974, Republic of Korea*

[3]*Institute for Materials Research, Tohoku University, Katahira 2-1-1, Sendai 980-8577, Japan*

[4]*Research Institute for Interdisciplinary Science, Okayama University, Okayama 700-8530, Japan*

[5]*Materials Science Division, Argonne National Laboratory, Argonne, Illinois 60439, USA*

(Received 14 November 2023; accepted 22 March 2024; published 5 April 2024)

We report on Raman scattering and ^{23}Na nuclear magnetic resonance (NMR) investigations of $j_{\rm eff} = 1/2$ hyperkagome antiferromagnet $Na_{4-x}Ir_3O_8$, which lies in the Mott insulating state. Our Raman scattering experiments unveil remarkable parallels between the magnetic excitations of the pristine $Na_4Ir_3O_8$ and the Kitaev honeycomb material Na_2IrO_3, which are characterized by dominant fractional spinon excitations. In the case of moderate Na-deficient $Na_{4-x}Ir_3O_8$, however, a substantial suppression of the magnetic excitations is observed, alluding to the notable influence of charge fluctuations on spin dynamics. In addition, our site-specific ^{23}Na NMR measurements offer further insights into the spin dynamics when a minor concentration of holes is introduced into a spin-orbit coupled Mott insulator. Specifically, the spin-lattice relaxation rate $1/T_1$ reveals the emergence of pseudogaplike correlations at the Na(2) site, alongside a critical slowing down behavior at the Na(1) and Na(3) sites. These findings showcase the intricate interplay between itinerant holes and magnetic correlations in a spin-liquid-like background.

DOI: 10.1103/PhysRevB.109.144405

I. INTRODUCTION

Over the past few decades, spin-orbit-coupled (SOC) Mott iridates have garnered considerable attention due to their potential for realizing novel electronic and magnetic states [1]. Specifically, half-filled Mott insulating iridates with a low-spin ($5d^5$) configuration can stabilize a SO entangled $j_{\rm eff} = 1/2$ Kramers doublet when a delicate balance is achieved between strong SOC, on-site Coulombic interactions, electronic correlations, and crystal field effects [2]. In honeycomb or hyperkagome lattices built from edge-sharing IrO_6 octahedra, the $j_{\rm eff} = 1/2$ Ir^{4+} ions can accommodate bond-dependent anisotropic Kitaev interactions that engender quantum spin liquids (QSLs) [3–5].

The paradigmatic instances encompass the honeycomb iridates A_2IrO_3 (A = Na, Li, Cu) and their three-dimensional derivatives β- and γ-Li_2IrO_3 [6–11], along with the hyperkagome iridate $Na_4Ir_3O_8$ [12]. The honeycomb and hyperhoneycomb iridates are in close proximity to Kitaev spin liquids, which bear signatures of Majorana fermions and can be effectively described by an extended Kitaev model. However, for a hyperkagome antiferromagnet, determining its exact ground state remains unsettled, with potential possibilities including a 120° coplanar magnetic order, nematic valence bond solid, and QSL [13–26].

$Na_4Ir_3O_8$ constitutes a rare example of a $j_{\rm eff} = 1/2$ hyperkagome antiferromagnet, where Ir^{4+} ions form a three-dimensional network of corner-sharing triangles [12]. This hyperkagome iridate exhibits a large Curie–Weiss temperature of $\Theta_{\rm CW} \approx -480$ K and a low spin-freezing temperature $T_{\rm f} \sim 6$–7 K, indicating a high degree of magnetic frustration. Remarkably, the huge Wilson ratio $W_{\rm L} \sim 30$ and the divergence of the magnetic Grüneisen parameter as $T \to 0$ K allude to an inherent instability towards a magnetically ordered state from a putative QSL [24,27]. Subsequent investigations using μSR and nuclear magnetic resonance (NMR) techniques have identified the occurrence of a quasistatic spin-frozen state at $T_{\rm f}$ [28,29]. Moreover, a recent single-crystal x-ray diffraction (XRD) study revealed $q = (1/3, 1/3, 1/3)$ superlattice peaks, speculated to arise from the sodium ordering of nominally disordered crystallographic Na(2) and Na(3) sites with 75% occupancy [see Fig. 1(a) for Na environments] [30].

In addition, $Na_4Ir_3O_8$ offers another intriguing aspect, as Na-deficient samples $Na_{4-x}Ir_3O_8$ introduce hole doping into the $j_{\rm eff} = 1/2$ bands that comprise the t_{2g} complex of predominantly Ir $5d$ character [20,31,32]. Even in the presence of Na deficiency the hyperkagome network of IrO_6 octahedra remains intact [33–39]. It is known that the SOC-assisted Mott state with significant antiferromagnetic interactions persists up to $x = 0.3$ [33]. However, for Na deficiency levels of $x \geqslant 0.7$, $Na_{4-x}Ir_3O_8$ displays a semimetallic state, which is owed to the competition between the formation of molecular orbitals on the Ir3 triangles [marked in Fig. 1(a)] and the suppression of the band gap due to the creation of a $j_{\rm eff} = 1/2$-like state. The related issue that requires further

*These authors contributed equally to this work.
†nojiri@imr.tohoku.ac.jp
‡mitchell@anl.gov
§choisky99@skku.edu

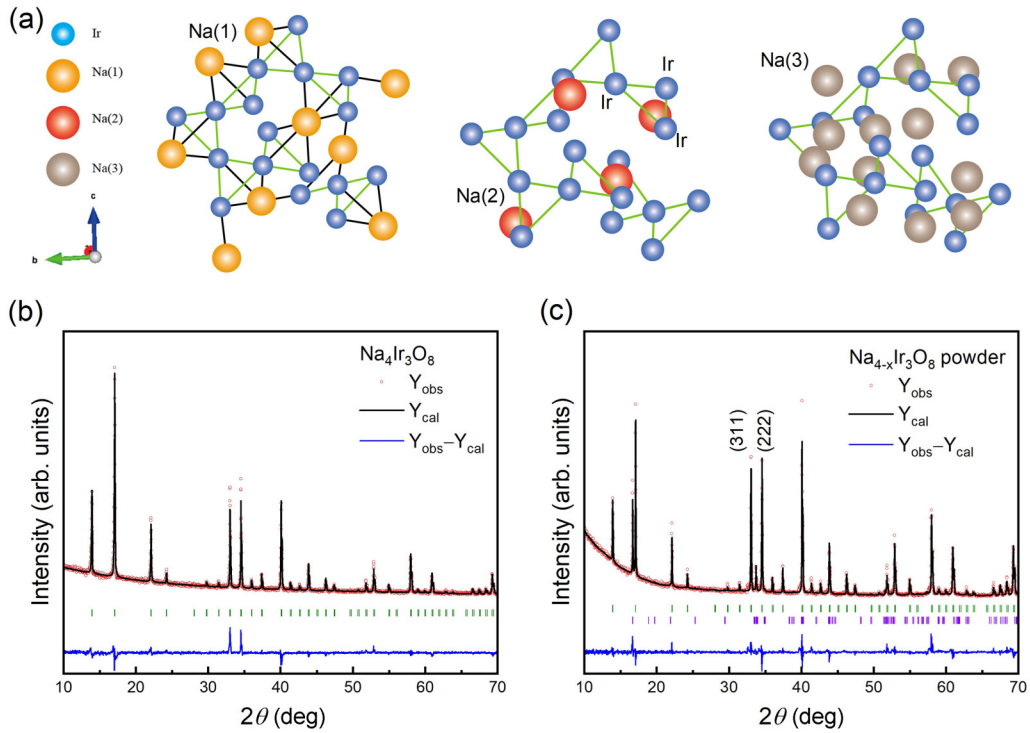

FIG. 1. (a) Crystal structure of $Na_4Ir_3O_8$ with three different Na sites. The blue, yellow, red, and gray spheres represent Ir, Na(1), Na(2), and Na(3) atoms, respectively. The oxygen atoms are omitted for clarity. Na(1) is connected to three Ir to form the Ir3Na tetrahedra. Na(2) and Na(3) also constitute a network of corner-shared tetrahedra, each having a 75% occupancy. XRD pattern of the ground single crystals of (b) $Na_4Ir_3O_8$ and (c) $Na_{4-x}Ir_3O_8$. The observed, calculated, and difference patterns are denoted by the red circles and black and blue lines, respectively. The diffraction peaks for $Na_4Ir_3O_8$ and Na_2IrO_3 are marked with the respective green and purple bars beneath the XRD patterns.

clarification is to understand the spin dynamics of mobile holes in the quasistatic ordered background with QSL-like fluctuations.

In this study, we combine Raman scattering and ^{23}Na NMR techniques towards comprehending low-energy excitations and a magnetic ground state of $Na_{4-x}Ir_3O_8$, located in the Mott insulating state. The Raman spectrum of $Na_4Ir_3O_8$ exhibits spinonlike fractional excitations. In the case of slightly Na-deficient $Na_{4-x}Ir_3O_8$, the magnetic Raman excitation is substantially suppressed. Furthermore, ^{23}Na NMR measurements reveal the local development of pseudogaplike magnetic correlations at the Na(2) site. All these results demonstrate the site-specific impact of itinerant holes on spin dynamics in the SOC Mott insulator $Na_{4-x}Ir_3O_8$.

II. EXPERIMENTAL DETAILS

Single crystals of $Na_4Ir_3O_8$ were grown at Argonne National Laboratory as detailed in Ref. [30], while single crystals of $Na_{4-x}Ir_3O_8$ were synthesized at IMR, Tohoku University, Japan. The synthesis procedure of single crystals involved two steps: initial sealing of an aluminum oxide tube using the xenon lamp floating zone furnace, followed by vapor crystal growth. To assess the sample quality, powder XRD measurements were carried out with Cu $K\alpha$ radiation (a D8-advanced model). The magnetic susceptibilities were measured using a vibrating sample magnetometer (Quantum Design MPMS and VSM). As-made crystals comprise a few large crystals (approximately 1 mm in size) and numerous tiny fragments (around 100 μm). Due to the rapid decomposition of $Na_{4-x}Ir_3O_8$ materials in air, variations in sample loading time into cryostat hindered us from conducting all measurements for the same composition x. For this reason, it is needed to specify the sample used in each experiment. First, three distinct large pieces were utilized for SQUID (designated as crystal 1), Raman (crystal 2), and NMR (crystal 3) experiments. After these characterizations, XRD measurements were made with ground samples consisting of many small pieces and two large crystals (sc + crystal 1 + crystal 2). Here, "sc" refers to small crystal fragments of 100 μm in size.

Raman scattering experiments were performed in the backscattering geometry using a DPSS SLM laser with an excitation line $\lambda = 532$ nm. The laser beam with a power of $P = 100$ μW was focused onto the crystal surface using a ×40 magnification microscope objective, resulting in a few-micrometer-diameter spot. The scattered spectra were collected using a micro-Raman spectrometer (XperRama200VN, Nanobase) with an air-cooled charge-coupled device (Andor iVac Camera). To reject Rayleigh scattering, a notch filter was employed with a lower cutoff frequency of 15 cm^{-1}. The temperature is varied from 5 to 400 K using a liquid-He-cooled continuous flow cryostat.

^{23}Na ($I = 3/2$, $^{23}\gamma_N = 11.26$ MHz/T) NMR measurements were conducted using a MagRes spectrometer and a 14 T Oxford Teslatron superconducting magnet. An external magnetic field was applied along the ab plane of the single crystalline sample $Na_{4-x}Ir_3O_8$. The NMR spectra were acquired using a silver Ag coil due to the similar

gyromagnetic ratios of ^{23}Na and ^{63}Cu ($^{63}\gamma_N$ = 11.319 MHz/T). We obtained ^{23}Na NMR spectra by a fast Fourier transform of spin-echo signals with a $\pi/2$-pulse length of $\tau_{\pi/2} = 1.5$ μs. The nuclear spin-lattice relaxation time T_1 was measured by the standard saturation recovery technique with multiple saturation pulse ($[\pi/2]_x - t$-$\pi/2$-π) with a $\pi/2$ pulse length of $\tau_{\pi/2} = 1.5$–2 μs. The recovery function of the nuclear magnetization curve $M(t)$ for $I = 3/2$ nuclei with elapsed time t is given by the following equation:

$$\frac{M_\infty - M(t)}{M_\infty} = A[0.9e^{-(6t/T_1^*)^\beta} + 0.1e^{-(t/T_1^*)^\beta}],$$

where A is a fitting parameter and β is the stretched exponent. Further analysis of $M(t)$ was made using the inverse Laplace transform (ILT) method based on Tikhonov regularization [40]: $M(t) = \sum_i P(1/T_{1i})[1 - 2\exp(-t/T_{1i})]$, where $P(1/T_{1i})$ represents the histogram of $1/T_{1i}$ subject to the condition $\sum_i P(1/T_{1i}) = 1$ and $1/T_{1i}$ is the ith value of the distributed $1/T_1$. We stress that the ILT analysis is concerned with obtaining the distribution of relaxation times by describing $M(t)$ as a combination of exponential decay components, while the stretched exponential fit estimates the average value within a distribution of T_1 times.

III. RESULTS AND DISCUSSION

A. XRD and magnetic susceptibility

Figures 1(b) and 1(c) compare the powder XRD patterns of $Na_4Ir_3O_8$ and $Na_{4-x}Ir_3O_8$ samples. The XRD data for $Na_4Ir_3O_8$ were reproduced from Ref. [30], in which the authors of our study are involved. Contrary to the pristine $Na_4Ir_3O_8$, it turns out that powder $Na_{4-x}Ir_3O_8$ contains 6.15% of Na_2IrO_3 impurities, as indicated by the purple bars in Fig. 1(c). These impurities were likely included during the preparation process for the XRD measurements, where small and large crystals (sc + crystal 1 + crystal 2) were ground together. Unlike the larger crystal pieces (crystal 1 and crystal 2), the tiny Na_2IrO_3 by-products could not be entirely eliminated from the smaller pieces. Upon closer inspection on the intensity of the (222) and (311) peaks, we find that $Na_{4-x}Ir_3O_8$ suffers from a certain degree of Na deficiency [28]. Nonetheless, Rietveld refinement reveals that both $Na_4Ir_3O_8$ and $Na_{4-x}Ir_3O_8$ samples possess the $P4_132$ space group with the identical lattice parameter of $a = 8.9885$ Å. Notably, the lattice parameters remain unaltered despite the reduction of the Na(2) occupancy. A comparison to existing literature [33] shows that the studied $Na_{4-x}Ir_3O_8$ resides on the Mott insulating side ($x < 0.3$). We stress that the estimated x from the XRD data should be regarded as an upper limit because the large crystals employed for SQUID and Raman measurements were reused.

In Fig. 2, we present the magnetic susceptibilities $\chi(T)$ of $Na_4Ir_3O_8$ (blue line), $Na_{4-x}Ir_3O_8$ (crystal 1; pink circles), and Na_2IrO_3 (emerald squares). The hyperkagome related compounds show a clear signature of quasistatic order at $T_f = 6$ K, as zoomed in the inset of Fig. 2. Compared to $Na_4Ir_3O_8$, the $\chi(T)$ of $Na_{4-x}Ir_3O_8$ is reduced by approximately 10%. By fitting the $\chi(T)$ data with a Curie-Weiss model in the temperature range of $T = 150$–300 K, we obtain the Curie-Weiss temperatures $\Theta_{CW} = -472$ and -484 K and the effective magnetic moments 1.82 and 1.93μ_B for $Na_4Ir_3O_8$ and $Na_{4-x}Ir_3O_8$ samples, respectively. By comparing our $\chi(T)$ data with those in Ref. [33], we deduce that x of crystal 1 is unlikely to exceed 0.1. Furthermore, it is worth emphasizing that $\chi(T)$ of $Na_{4-x}Ir_3O_8$ reveals no discernible trace of Na_2IrO_3 in contrast to the XRD pattern. This disparity is due to the fact that we initially used a single large piece of $Na_{4-x}Ir_3O_8$ for SQUID measurements, ensuring their purity without any impurities.

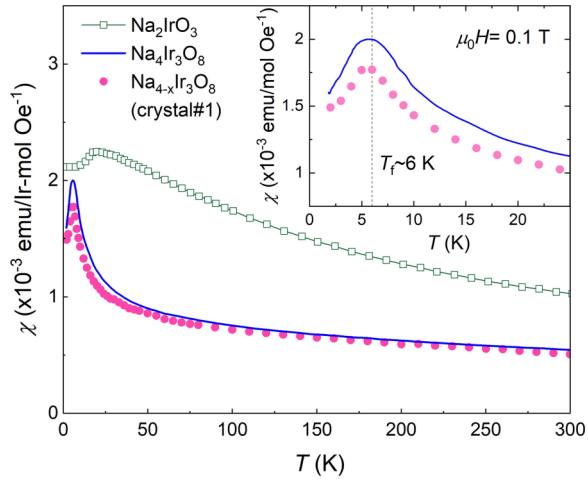

FIG. 2. Temperature dependence of the magnetic susceptibility $\chi(T)$ for $Na_4Ir_3O_8$ (blue line), $Na_{4-x}Ir_3O_8$ (pink circles; crystal 1), and Na_2IrO_3 (emerald squares) measured under a magnetic field of $\mu_0 H = 0.1$ T. The inset zooms in on the low-temperature magnetic susceptibility, indicative of a spin-frozen transition at $T_f = 6$ K.

B. Raman spectra

To obtain a deeper understanding of the low-lying excitations in a hyperkagome lattice, we begin by comparing the Raman spectra of honeycomb and hyperkagome iridates, including Na_2IrO_3, $Na_4Ir_3O_8$, and $Na_{4-x}Ir_3O_8$ that share tricoordinated lattices.

Figure 3 compares the Raman spectra of the three iridates measured in (xx) polarization at temperatures of $T = 5$ and 280 K. In the case of Na_2IrO_3, we resolve eight first-order phonon peaks at 188, 214, 396, 417, 460, 494, 569, and 618 cm^{-1}. These phonon peaks are part of the 15 Raman-active phonons $\Gamma_{Raman} = 7A_g + 8B_g$ predicted for the monoclinic $C2/m$ space group. Notably, we find similarities in phonon energies between the isostructural Na_2IrO_3 and α-Li_2IrO_3 [compare Fig. 3(a) and Fig. 1(c) in Ref. [41]]. In addition to the phonon excitations, we also observe a broad background of magnetic excitations (color shadings), which extends up to approximately 800 cm^{-1}. For energies above 300 cm^{-1}, the higher-energy magnetic continuum undergoes little variation with temperature. On the other hand, the magnetic background scattering below 300 cm^{-1} shows a notable increase at elevated temperatures. We stress that the systematic thermal variation of the background is not compatible with the possibility that a phonon density of states contributes to the background scattering.

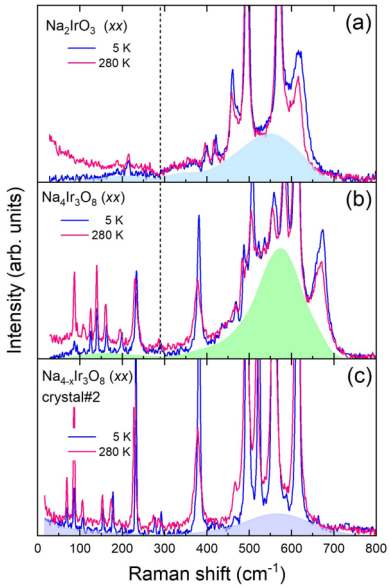

FIG. 3. Comparison of the Raman spectra between Na_2IrO_3 (upper), $Na_4Ir_3O_8$ (middle), and $Na_{4-x}Ir_3O_8$ (lower panel; crystal 2) in (xx) polarization at temperatures of $T = 5$ and 280 K. The color shadings denote magnetic excitations.

Next, we turn to the hyperkagome iridates. For the $P4_132$ space group, factor group analysis predicts a total of 44 Raman-active modes: $\Gamma_{\text{Raman}} = 6A_1(aa, bb, cc) + 16E(aa, bb, cc) + 22T_2(ab, ac, bc)$. Actually, we observe 22 and 20 phonons for $Na_4Ir_3O_8$ and $Na_{4-x}Ir_3O_8$ (crystal 2), respectively, which closely match the 22 symmetry-allowed modes in the (xx) scattering channel. The Na deficiency is known to increase distortions of IrO_6 octahedra due to the depletion of Na^+ ions that share the pyrochlore lattice with Ir^{4+} ions [32]. This enhanced octahedral distortion gives a rationale for the increasing phonon scattering intensity without causing appreciable broadening in $Na_{4-x}Ir_3O_8$ [see Fig. 3(c)]. In contrast to the phonon spectra, Na-deficient $Na_{4-x}Ir_3O_8$ exhibits a significant change in the magnetic background marked by the purple shading in Fig. 3(c). First, the higher-energy continuum is appreciably suppressed. Second, the lower-energy excitation features a weak quasielastic response even at temperatures as low as $T = 5$ K. This suggests that the introduction of mobile holes renders coherent magnetic excitations incoherent.

To shed light on the temperature-dependent behavior of magnetic excitations, we present the Raman spectra in Figs. 4(a)–4(c) and the corresponding phonon-subtracted spectra in Figs. 4(d)–4(f). Our primary focus is on the broad magnetic continuum beneath the phonon peaks. Initially, the sharp phonon features were modeled as a sum of Lorentzian profiles. Within a narrow fitting frequency range, we approximate the baselines of Lorentzian profiles as a piecewise linear function. Subsequently, we take into account the difference between the raw spectra and the superimposed Lorentzian lines and piecewise linear background. Finally, we optimize the goodness of fit to fine-tune the structured background.

As is evident from Figs. 4(a) and 4(d), the honeycomb iridate Na_2IrO_3 exhibits a dichotomic thermal behavior in its magnetic excitations: two prominent phenomena emerge within different energy ranges. First, the lower-energy magnetic excitation in the spectral range of $\omega = 20$–300 cm^{-1} experiences a gradual development of quasielastic scattering with increasing temperature. This behavior can be attributed to a paramagnonlike response, arising from the dissolution of a long-range magnetic order upon heating above 15 K.

Second, the higher-energy broad continuum centered at 596 cm^{-1} exhibits stronger intensity compared to the lower-energy counterpart, with a cutoff energy $\omega_{hc} \approx 800$ cm^{-1} roughly twice that of the lower-energy excitations. Notably, as the temperature increases, the spectral form of the high-energy continuum remains largely unchanged, albeit with a slight reduction in scattering intensity. These characteristics are fundamentally different from the typical thermal evolution of two-magnon excitations, which typically display a rapid increase in integrated scattering intensity and a thermal damping of spectral weight at high temperatures [42]. In this regard, the quasiparticles of Na_2IrO_3 in the high-energy regime are not described by magnons. Given the proximity of Na_2IrO_3 to a QSL state [43], we attribute the higher-energy continuum to a multispinonlike response. In the spin-conserving Raman scattering process, excitations involving spinon-antispinon pairs are prominent over single particle excitations permitted by SOC. Additionally, the density of states associated with spinon pair excitations is twice that of single particle excitations. The low-energy magnonlike response contributes only a minor fraction to the total spectral weight, consistent with the characteristics of a proximate spin-liquid phase. Our interpretation is supported by resonant inelastic x-ray scattering (RIXS) studies, which reveal Majorana fermionic excitations centered around 280 cm^{-1} and extending up to 800 cm^{-1} [44,45]. It is worth noting that the peak energy of the RIXS spectrum is half that of the high-energy continuum observed in the Raman spectra. This discrepancy in peak energies can be attributed to the distinct scattering processes: while multiquasiparticle Raman scattering primarily involves spin-conserving processes, RIXS is dominated by single-spin-flip processes.

Figures 4(b) and 4(e) plot the temperature dependence of magnetic excitations in $Na_4Ir_3O_8$. We find striking similarities between $Na_4Ir_3O_8$ and Na_2IrO_3 in the spectral form, width, and energy scale of their magnetic excitations despite their different spin lattices and exchange interactions. This intriguing resemblance prompts us to interpret the higher-energy excitation as spinonlike and the lower-energy excitation as magnonlike. Accordingly, we conjecture that the persistence of short-range correlations up to quite high temperatures may be indicative of a nearby QSL state.

Upon closer inspection, it becomes apparent that the quasielastic scattering at higher temperatures is less pronounced in $Na_4Ir_3O_8$ compared to Na_2IrO_3, indicating that the low-energy excitation in $Na_4Ir_3O_8$ carries more pronounced spin-liquid-like correlations than its counterpart in Na_2IrO_3. It is worth noting that the calculated spin dynamical structure factor displays a broad continuum ranging from $\omega = 0$ to $1.1J$, with significant spectral weight at $\omega = 0.3$ and $0.8J$ [46]. In spin-conserving Raman processes, strong magnetic Raman signals are anticipated at $\omega = 0.6$ and $1.6J$, corresponding to the peak energy of the low- and high-energy

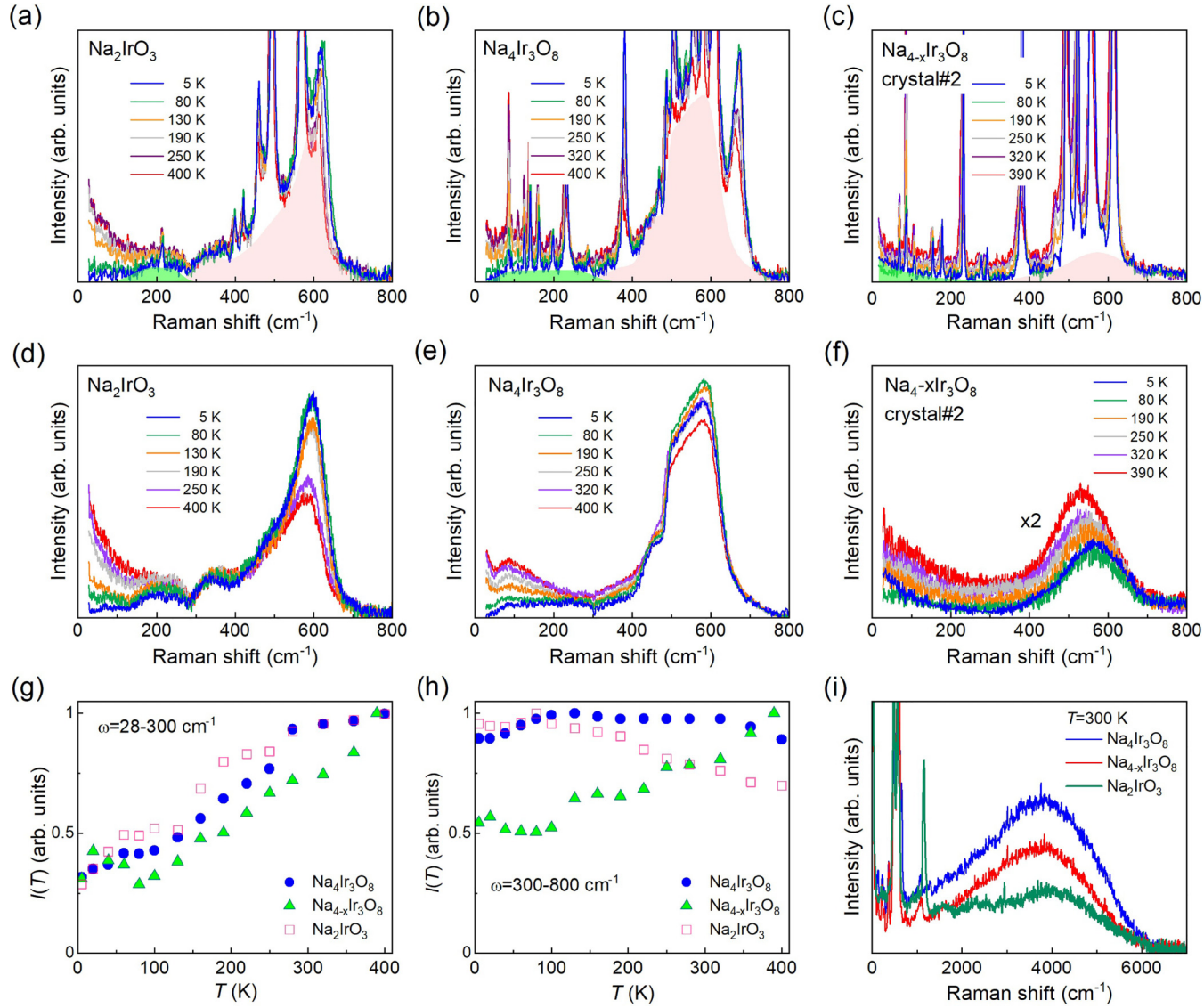

FIG. 4. Temperature dependence of the Raman spectra for (a) Na_2IrO_3, (b) $Na_4Ir_3O_8$, and (c) $Na_{4-x}Ir_3O_8$ (crystal 2). Thermal evolution of magnetic excitations obtained by subtracting phonon peaks for (d) Na_2IrO_3, (e) $Na_4Ir_3O_8$, and (f) $Na_{4-x}Ir_3O_8$ (crystal 2). Temperature dependence of the low- and high-energy magnetic scattering intensity integrated over the frequency range (g) $\omega = 28$–300 cm^{-1} and (h) $\omega = 300$–800 cm^{-1} for Na_2IrO_3 (red squares), $Na_4Ir_3O_8$ (blue circles), and $Na_{4-x}Ir_3O_8$ (green triangles; crystal 2). The intensities are normalized to the $T = 400$ K data. (i) Spin-orbit excitons of Na_2IrO_3, $Na_4Ir_3O_8$, and $Na_{4-x}Ir_3O_8$ (crystal 2) measured at room temperature.

excitations at approximately 200 and 560 cm^{-1}, respectively. This comparison enables us to estimate the value of J as 476–500 K, which is larger than $J \sim 300$ K obtained from a high-temperature series expansion [47].

We now turn our attention to the thermal behavior of magnetic excitations in Na-deficient $Na_{4-x}Ir_3O_8$ (crystal 2), as depicted in Figs. 4(c) and 4(f). Compared to the pristine $Na_4Ir_3O_8$, the spectral form and range of magnetic excitations remain largely unaltered, except for a notable reduction in scattering intensity. This implies that the strength of magnetic interactions is minimally affected by the site-specific removal of Na(2) ions and accompanying distortions in IrO_6 octahedra [33–39]. As plotted in Figs. 4(g) and 4(h), the low-energy scattering intensity for the studied iridates displays a quasilinear increment up to 250 K, followed by saturation. Conversely, the higher-energy scattering intensity of Na-deficient $Na_{4-x}Ir_3O_8$ exhibits an opposing trend to that of $Na_4Ir_3O_8$ and Na_2IrO_3. The increasing intensity with temperature mainly arises from the systematic leveling up of background signal. Taken together, the primary impact of Na deficiency on magnetic excitations is the overall suppression of scattering intensity and the systematic increase in background signal, stemming from scatterings of magnetic excitations by mobile holes: local charge fluctuations shorten the lifetime of magnetic excitations and disturb their coherence.

Lastly, we focus on a broad Raman continuum centered around 3500 cm^{-1} with a bandwidth of 1700 cm^{-1} that was previously discussed in terms of fractionalized magnetic vs electronic excitations [48]. In a similar energy range, the

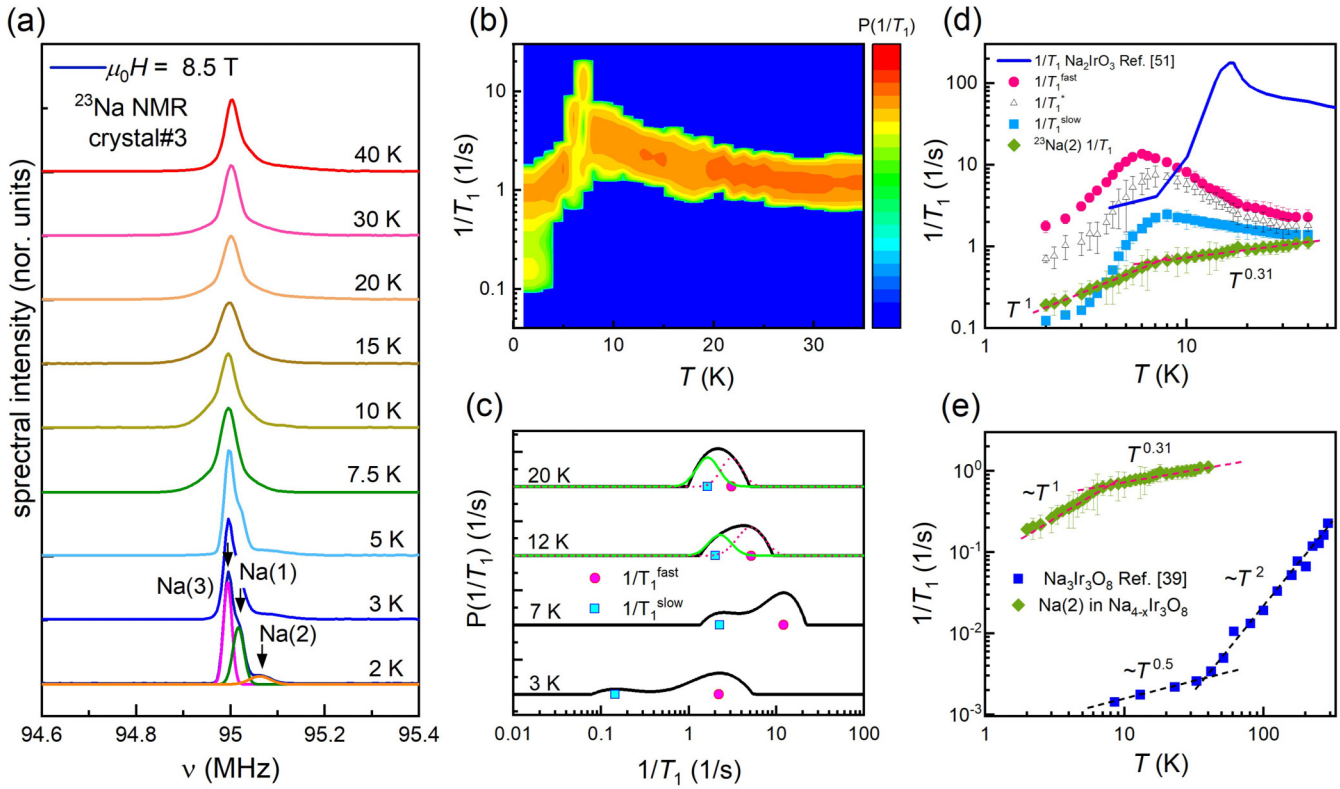

FIG. 5. (a) Temperature dependence of ^{23}Na NMR spectra for $Na_{4-x}Ir_3O_8$ measured at an external field of $\mu_0H = 8.5$ T. (b) The color contour plot of the histogram $P(1/T_1)$ in the temperature-$1/T_1$ plane. (c) Distribution function $P(1/T_1)$ as selected temperatures. The symbols mark two components of $1/T_1^{slow}$ (pink circles) and $1/T_1^{fast}$ (green squares). The red dotted and green solid lines are representative of two Gaussian fits. (d) Log-log plot of the ^{23}Na spin-lattice relaxation rates: $1/T_1^{fast}$ (pink circles), $1/T_1^{slow}$ (azure squares), $1/T_1^{*}$ (open triangles), and $1/T_1$ for Na(2) (green diamonds). The blue line represents $1/T_1$ of Na_2IrO_3 taken from Ref. [51]. The dashed lines are fits to the power-law dependence $1/T_1 \sim T^n$. (e) Comparison of $1/T_1$ between $Na_{4-x}Ir_3O_8$ [for Na(2)] and $Na_3Ir_3O_8$.

studied three iridates feature commonly broad excitations extending to 6000 cm^{-1}, as shown in Fig. 4(i). Furthermore, the antiflurite K_2IrCl_6 whose magnetic energy scale does not exceed 10 K also shows a similar excitation, rendering a magnetic origin improbable [49]. Instead, we assign it to a SO exciton characteristic of a SO entangled $j_{\text{eff}} = 1/2$ insulator [50].

C. ^{23}Na NMR

Previous NMR studies on the pristine hyperkagome lattice $Na_4Ir_3O_8$ and its 1/3 hole-doped counterpart $Na_3Ir_3O_8$ have demonstrated the effectiveness of the ^{23}Na nucleus as a probe for investigating intrinsic hyperkagome physics [29,35,39]. For $Na_4Ir_3O_8$, the ^{23}Na and ^{17}O NMR results revealed a static disordered spin freezing occurring at T_f, along with a spin-liquid behavior at higher temperatures. On the other hand, $Na_3Ir_3O_8$ displayed the persistence of antiferromagnetic correlations into a semimetallic state. Based on these previous investigations, we focus on a slightly depleted sample $Na_{4-x}Ir_3O_8$ to address low-energy spin correlations that emerge when introducing a small amount of holes into a spin-liquid background.

In Fig. 5(a), we present a cascade plot of the ^{23}Na NMR spectra of $Na_{4-x}Ir_3O_8$ (crystal 3) at selected temperatures of $T = 2$–40 K. Noticeably, we observe three distinct NMR lines, which are in accordance with the three crystallographically inequivalent Na sites in the structure [see Fig. 1(a) for three Na environments]. The relative integrated intensities of these NMR peaks have the ratios 1:0.69:0.13 from the leftmost peak. Given the Na(1), Na(2), and Na(3) sites have ratios of 4:3:9 in $Na_4Ir_3O_8$, we attribute the three peaks to the Na(3), Na(1), and Na(2) sites from left to right. Our site assignment is in line with that reported in Ref. [29]. Compared to the pristine sample, the spectral weight of the Na(2) signal is diminished in the Na-deficient sample, which is due to the rearrangement of Na atoms induced by a Na^+ deficiency. More specifically, the primary structural change involves the removal of the Na(2) and Na(3) sites, with the occupancy of the Na(2) site being more significantly reduced compared to the Na(3) site [32,33]. However, the depletion of the Na(2) site exerts a minimal influence on magnetism because the Na(2) site pertains to the tetrahedral A site of spinel structure and the hyperkagome spin lattice of Ir moments is not disturbed.

With increasing temperature, the NMR spectrum undergoes a broadening and overlap of peaks down to T_f, which poses challenges in differentiating individual peaks. This intriguing temperature evolution of the spectrum is likely linked to the different hyperfine coupling constants A_{hf} between the ^{23}Na nuclear spins and the Ir^{4+} electron spins at each Na site. Consequently, tracking the NMR shift and linewidth as a function of temperature is not straightforward. Nevertheless,

it is evident that, upon cooling through T_f, the NMR spectrum exhibits a narrowing, accompanied by a modest decrease in its intensity. Specifically, the intensity of the NMR signal in the spin-frozen state diminishes to ∼85% of the intensity observed in the paramagnetic state. Considering the significant distribution of $1/T_1$ values depicted in Figs. 5(b) and 5(b), this intensity suppression may be attributed to the appearance of rapid relaxation times, which wipe out portions of the NMR signal. From now on, we delve into the spin-lattice relaxation rate $1/T_1$, which senses the low-energy component of the **q**-integrated spin excitation spectrum at the NMR frequency ω_0. As the ^{23}Na(1) and ^{23}Na(3) NMR signals are closed spaced, we employed the ILT method that allows for deducing the histogram $P(1/T_{1i})$, representing the distribution of $P(1/T_{1i})$ values [40].

Figure 5(b) showcases the color contour plot of $P(1/T_{1i})$ in the temperature-$1/T_1$ plane. By deconvoluting $P(1/T_{1i})$ into two Gaussian profiles as depicted Fig. 5(c), we are able to extract the temperature dependence of two distinct relaxation rates: $1/T_1^{\text{fast}}$ (pink circles) and $1/T_1^{\text{slow}}$ (azure squares), which are plotted in Fig. 5(d). On cooling from 40 K, $1/T_1^{\text{fast}}$ and $1/T_1^{\text{slow}}$ show a common increase until reaching a temperature of around 7 K, forming a maximum at the spin-freezing temperature T_f. Subsequently, at temperatures below 7 K, both $1/T_1$'s undergo a substantial drop by one order of magnitude, which is a characteristic behavior of the critical slowing down of magnetic fluctuations that occurs when entering a spin-frozen state. We note that $1/T_1^*$ [open triangles in Fig. 5(d)], obtained from the conventional stretched exponential analysis, matches the average of $1/T_1^{\text{fast}}$ and $1/T_1^{\text{slow}}$, validating the reliability of our ILT analysis used to derive the individual relaxation rates. Besides, the comparison of $1/T_1$'s between $Na_{4-x}Ir_3O_8$ (crystal 3) and Na_2IrO_3 [blue line in Fig. 5(d) and Ref. [51]] advocates that spin dynamics of $Na_{4-x}Ir_3O_8$ is not affected by the Na_2IrO_3 impurity.

Unlike the NMR peaks Na(1) and Na(3), the Na(2) line is separated from other peaks, enabling us to determine a well-defined relaxation rate. As plotted in Fig. 5(d), $1/T_1$ for Na(2) (green diamonds) exhibits two distinct power-law regimes: a power-law decrease $T^{0.98\pm0.03}$ below T_f and $T^{0.31\pm0.02}$ above T_f. Singularly, the pseudogaplike suppression of ^{23}Na(2) $1/T_1$ observed below 40 K is contrasted by the critical-like divergent behavior observed in ^{23}Na(1) and ^{23}Na(3) $1/T_1$'s. We recall that the pseudogaplike behavior is often observed in QSL candidates such as κ-$(ET)_2Cu_2(CN)_3$ [52]. In such a system, the power-law decrease of $1/T_1$ with temperature is interpreted in terms of concurrent charge and spin fluctuations. In this light, the site-specific ^{23}Na NMR results highlight that spin dynamics probed at the Na(2) site is strongly affected by charge dynamics.

To elucidate the impact of charge fluctuations on magnetic correlations, we make a comparison of the relaxation rates between $Na_{4-x}Ir_3O_8$ [for Na(2) in Fig. 5(e)] and 1/3 hole-doped $Na_3Ir_3O_8$ [39]. The semimetallic iridate exhibits distinct temperature dependencies for the relaxation rates: a $1/T_1 \propto T^{1/2}$ behavior below ∼30 K and a T^2 behavior above 30 K. Remarkably, in the temperature range from 7 to 30 K, the ^{23}Na(2) $1/T_1$ value of $Na_{4-x}Ir_3O_8$ is nearly three orders of magnitude higher than that of $Na_3Ir_3O_8$. Furthermore, the exponent $\alpha = 0.5$ observed in $Na_3Ir_3O_8$ decreases to 0.31 in $Na_{4-x}Ir_3O_8$ for the Na(2) site. The qualitative similar yet quantitative disparate ^{23}Na(2) $1/T_1$ behavior suggests that the local-moment correlations are considerably stronger in $Na_{4-x}Ir_3O_8$, consistent with the presence of a much smaller hole doping concentration in this compound than the 1/3-doped $Na_3Ir_3O_8$. Additionally, we emphasize that the exponent changes from $\alpha = 0.31$ to ∼1 on cooling through T_f. This modified spin dynamics is a natural manifestation of the altering magnetic correlations that occur as the system enters the spin-frozen state.

IV. CONCLUSIONS

In conclusion, we have investigated the influence of hole carriers on the spin dynamics in Mott insulating $Na_{4-x}Ir_3O_8$ through combined Raman scattering and ^{23}Na NMR techniques. We initially map out magnetic excitations using inelastic light scattering. Our magnetic Raman spectra reveal striking similarities in the magnetic continuum between the pristine $Na_4Ir_3O_8$ and the Kitaev honeycomb material Na_2IrO_3 in its shape and energy. In both compounds, the lower-energy excitations below 300 cm^{-1} feature a magnonlike response, while the higher-energy excitations in the range of ω = 300–800 cm^{-1} are dominated by fractionalized excitations. The predominant spinonlike excitation gives evidence for the proximity to a QSL state. Upon introduction of hole carriers through doping in Na-deficient $Na_{4-x}Ir_3O_8$, a dampening and suppression of magnetic excitations occurs, signifying the influence of charge fluctuations on spin dynamics.

In addition, our site-specific ^{23}Na NMR measurements on $Na_{4-x}Ir_3O_8$ further illuminate the inhomogeneous development of magnetic correlations triggered by the introduction of charge carriers into a spin-liquid-like matrix. $1/T_1$'s at the Na(1) and Na(3) sites exhibit a critical slowing down, forming a maximum at T_f, which behave like the pristine sample. In sharp contrast, $1/T_1$ at the Na(2) site obeys a power-law decrease with decreasing temperature with the exponent $\alpha \sim 1$ below T_f and ∼0.31 above T_f. This pseudogaplike $1/T_1$ behavior highlights the modification of spin correlations by itinerant holes on spin correlations. Considering the Na(2) site is particularly susceptible to Na deficiency, the local moments near the Na(2) site are first affected by mobile holes. As a result, the influence of these charge carriers on spin dynamics is most pronounced in the proximity of the Na(2) site, especially when the system is located in the Mott insulating state. Our observations shed light on the evolution of pseudogaplike magnetic correlations within a hole-doped spin-frozen state in the SOC Mott insulating system $Na_{4-x}Ir_3O_8$.

ACKNOWLEDGMENTS

This work was supported by Korea Research Foundation (KRF) Grants (No. RS-2023-00209121 and No. 2020R1A5A1016518) funded by the Korea government (MEST) as well as by GIMRT(19G0504) in IMR, Tohoku University. Work in the Materials Science Division of

Argonne National Laboratory (crystal growth and characterization of $Na_4Ir_3O_8$) was supported by the U.S. Department of Energy, Office of Science, Basic Energy Sciences, Materials Science and Engineering Division.

[1] G. Cao and P. Schlottmann, The challenge of spin–orbit-tuned ground states in iridates: A key issues review, Rep. Prog. Phys. **81**, 042502 (2018).

[2] B. J. Kim, H. Jin, S. J. Moon, J.-Y. Kim, B.-G. Park, C. S. Leem, J. Yu, T. W. Noh, C. Kim, S.-J. Oh, J.-H. Park, V. Durairaj, G. Cao, and E. Rotenberg, Novel $J_{\rm eff} = 1/2$ Mott state induced by relativistic spin-orbit coupling in Sr_2IrO_4, Phys. Rev. Lett. **101**, 076402 (2008).

[3] A. Kitaev, Anyons in an exactly solved model and beyond, Ann. Phys. (NY) **321**, 2 (2006).

[4] G. Jackeli and G. Khaliullin, Mott insulators in the strong spin-orbit coupling limit: From Heisenberg to a quantum compass and Kitaev models, Phys. Rev. Lett. **102**, 017205 (2009).

[5] I. Kimchi and A. Vishwanath, Kitaev-Heisenberg models for iridates on the triangular, hyperkagome, kagome, fcc, and pyrochlore lattices, Phys. Rev. B **89**, 014414 (2014).

[6] Y. Singh and P. Gegenwart, Antiferromagnetic Mott insulating state in single crystals of the honeycomb lattice material Na_2IrO_3, Phys. Rev. B **82**, 064412 (2010).

[7] Y. Singh, S. Manni, J. Reuther, T. Berlijn, R. Thomale, W. Ku, S. Trebst, and P. Gegenwart, Relevance of the Heisenberg-Kitaev model for the honeycomb lattice iridates A_2IrO_3, Phys. Rev. Lett. **108**, 127203 (2012).

[8] Y. S. Choi, C. H. Lee, S. Lee, S. Yoon, W.-J. Lee, J. Park, A. Ali, Y. Singh, J.-C. Orain, G. Kim, J.-S. Rhyee, W.-T. Chen, F. C. Chou, and K.-Y. Choi, Exotic low-energy excitations emergent in the random kitaev magnet Cu_2IrO_3, Phys. Rev. Lett. **122**, 167202 (2019).

[9] K. A. Modic, T. E. Smidt, I. Kimchi, N. P. Breznay, A. Biffin, S. Choi, R. D. Johnson, R. Coldea, P. Watkins-Curry, G. T. McCandless, J. Y. Chan, F. Gandara, Z. Islam, A. Vishwanath, A. Shekhter, R. D. McDonald, and J. G. Analytis, Realization of a three-dimensional spin–anisotropic harmonic honeycomb iridate, Nat. Commun. **5**, 4203 (2014).

[10] T. Takayama, A. Kato, R. Dinnebier, J. Nuss, H. Kono, L. S. I. Veiga, G. Fabbris, D. Haskel, and H. Takagi, Hyperhoneycomb iridate β-Li_2IrO_3 as a platform for Kitaev magnetism, Phys. Rev. Lett. **114**, 077202 (2015).

[11] A. Glamazda, P. Lemmens, S.-H. Do, Y. S. Choi, and K.-Y. Choi, Raman spectroscopic signature of fractionalized excitations in the harmonic-honeycomb iridates β- and γ-Li_2IrO_3, Nat. Commun. **7**, 12286 (2016).

[12] Y. Okamoto, M. Nohara, H. Aruga-Katori, and H. Takagi, Spin-liquid state in the $S = 1/2$ hyperkagome antiferromagnet $Na_4Ir_3O_8$, Phys. Rev. Lett. **99**, 137207 (2007).

[13] J. M. Hopkinson, S. V. Isakov, H.-Y. Kee, and Y. B. Kim, Classical antiferromagnet on a hyperkagome lattice, Phys. Rev. Lett. **99**, 037201 (2007).

[14] Y. Zhou, P. A. Lee, T.-K. Ng, and F.-C. Zhang, $Na_4Ir_3O_8$ as a 3D spin liquid with fermionic spinons, Phys. Rev. Lett. **101**, 197201 (2008).

[15] G. Chen and L. Balents, Spin-orbit effects in $Na_4Ir_3O_8$: A hyper-kagome lattice antiferromagnet, Phys. Rev. B **78**, 094403 (2008).

[16] M. E. Zhitomirsky, Octupolar ordering of classical kagome antiferromagnets in two and three dimensions, Phys. Rev. B **78**, 094423 (2008).

[17] M. J. Lawler, A. Paramekanti, Y. B. Kim, and L. Balents, Gapless spin liquids on the three-dimensional hyperkagome lattice of $Na_4Ir_3O_8$, Phys. Rev. Lett. **101**, 197202 (2008).

[18] M. J. Lawler, H.-Y. Kee, Y. B. Kim, and A. Vishwanath, Topological spin liquid on the hyperkagome lattice of $Na_4Ir_3O_8$, Phys. Rev. Lett. **100**, 227201 (2008).

[19] D. Podolsky, A. Paramekanti, Y. B. Kim, and T. Senthil, Mott transition between a spin-liquid insulator and a metal in three dimensions, Phys. Rev. Lett. **102**, 186401 (2009).

[20] M. R. Norman and T. Micklitz, Electronic structure of hyperkagome $Na_4Ir_3O_8$, Phys. Rev. B **81**, 024428 (2010).

[21] T. Micklitz and M. R. Norman, Spin Hamiltonian of hyperkagome $Na_4Ir_3O_8$, Phys. Rev. B **81**, 174417 (2010).

[22] E. J. Bergholtz, A. M. Läuchli, and R. Moessner, Symmetry breaking on the three-dimensional hyperkagome lattice of $Na_4Ir_3O_8$, Phys. Rev. Lett. **105**, 237202 (2010).

[23] D. Podolsky and Y. B. Kim, Spin-orbit coupling in the metallic and spin-liquid phases of $Na_4Ir_3O_8$, Phys. Rev. B **83**, 054401 (2011).

[24] G. Chen and Y. B. Kim, Anomalous enhancement of the Wilson ratio in a quantum spin liquid: The case of $Na_4Ir_3O_8$, Phys. Rev. B **87**, 165120 (2013).

[25] T. Mizoguchi, K. Hwang, E. K.-H. Lee, and Y. B. Kim, Generic model for the hyperkagome iridate $Na_4Ir_3O_8$ in the local-moment regime, Phys. Rev. B **94**, 064416 (2016).

[26] B. Huang, Y. B. Kim, and Y.-M. Lu, Interplay of nonsymmorphic symmetry and spin-orbit coupling in hyperkagome spin liquids: Applications to $Na_4Ir_3O_8$, Phys. Rev. B **95**, 054404 (2017).

[27] Y. Singh, Y. Tokiwa, J. Dong, and P. Gegenwart, Spin liquid close to a quantum critical point in $Na_4Ir_3O_8$, Phys. Rev. B **88**, 220413(R) (2013).

[28] R. Dally, T. Hogan, A. Amato, H. Luetkens, C. Baines, J. Rodriguez-Rivera, M. J. Graf, and S. D. Wilson, Short-range correlations in the magnetic ground state of $Na_4Ir_3O_8$, Phys. Rev. Lett. **113**, 247601 (2014).

[29] A. C. Shockley, F. Bert, J.-C. Orain, Y. Okamoto, and P. Mendels, Frozen state and spin liquid physics in $Na_4Ir_3O_8$: An NMR study, Phys. Rev. Lett. **115**, 047201 (2015).

[30] H. Zheng, J. Zhang, C. C. Stoumpos, Y. Ren, Y.-S. Chen, R. Dally, S. D. Wilson, Z. Islam, and J. F. Mitchell, Controlled vapor crystal growth of $Na_4Ir_3O_8$: A three-dimensional quantum spin liquid candidate, Phys. Rev. Mater. **2**, 043403 (2018).

[31] D. Pröpper, A. N. Yaresko, T. I. Larkin, T. N. Stanislavchuk, A. A. Sirenko, T. Takayama, A. Matsumoto, H. Takagi, B. Keimer, and A. V. Boris, Fano resonances in the infrared spectra of phonons in hyperkagome $Na_3Ir_3O_8$, Phys. Rev. Lett. **112**, 087401 (2014).

[32] T. Takayama, A. Yaresko, A. Matsumoto, J. Nuss, K. Ishii, M. Yoshida, J. Mizuki, and H. Takagi, Spin-orbit coupling

induced semi-metallic state in the 1/3 hole-doped hyperkagome $Na_3Ir_3O_8$, Sci. Rep. **4**, 6818 (2014).

[33] A. Balodhi, A. Thamizhavel, and Y. Singh, Evolution of magnetic, transport, and thermal properties in $Na_{4-x}Ir_3O_8$, Phys. Rev. B **91**, 224409 (2015).

[34] B. Fauque, X. Xu, A. F. Bangura, E. C. Hunter, A. Yamamoto, K. Behnia, A. Carrington, H. Takagi, N. E. Hussey, and R. S. Perry, Thermal conductivity across the metal-insulator transition in the single-crystalline hyperkagome antiferromagnet $Na_{3+x}Ir_3O_8$, Phys. Rev. B **91**, 075129 (2015).

[35] S. Yoon, S.-H. Baek, A. Balodhi, W.-J. Lee, K.-Y. Choi, I. Watanabe, J. S. Lord, B. Büchner, B. J. Suh, and Y. Singh, Spin dynamics in $Na_{4-x}Ir_3O_8$(x=0.3 and 0.7) investigated by ^{23}Na NMR and μSR, J. Phys.: Condens. Matter **27**, 485603 (2015).

[36] M. V. Talanov, V. B. Shirokov, and V. M. Talanov, Unique hyper-kagome atomic order in the noncentrosymmetric structure of $Na_3Ir_3O_8$, Inorg. Mater. **52**, 815 (2016).

[37] F. Sun, H. Zheng, Y. Liu, E. D. Sandoval, C. Xu, J. Xu, C. Q. Jin, C. J. Sun, W. G. Yang, H. K. Mao, J. F. Mitchell, A. N. Kolmogorov, and D. Haskel, Electronic and structural response to pressure in the hyperkagome-lattice $Na_3Ir_3O_8$, Phys. Rev. B **98**, 085131 (2018).

[38] T. Takayama, A. N. Yaresko, A. S. Gibbs, K. Ishii, D. Kukusta, and H. Takagi, Robust spin-orbit coupling induced semimetallic state in hyperkagome iridate $Li_3Ir_3O_8$, Phys. Rev. Mater. **4**, 075002 (2020).

[39] G. Simutis, T. Takayama, Q. Barthélemy, F. Bert, H. Takagi, and P. Mendels, Magnetic correlations in the semimetallic hyperkagome iridate $Na_3Ir_3O_8$, Phys. Rev. B **103**, L100404 (2021).

[40] P. M. Singer, A. Arsenault, T. Imai, and M. Fujita, ^{139}La NMR investigation of the interplay between lattice, charge, and spin dynamics in the charge-ordered high-T_c cuprate $La_{1.875}Ba_{0.125}CuO_4$, Phys. Rev. B **101**, 174508 (2020).

[41] G. Li, L.-L. Huang, X. Chen, C. Liu, S. Pei, X. Wang, S. Wang, Y. Zhao, D. Yu, L. Wang, F. Ye, J.-W. Mei, and M. Huang, Probing the continuum scattering and magnetic collapse in single-crystalline α-Li_2IrO_3 by Raman spectroscopy, Phys. Rev. B **101**, 174436 (2020).

[42] D. Wulferding, Y. Choi, W. Lee, and K.-Y. Choi, Raman spectroscopic diagnostic of quantum spin liquids, J. Phys.: Condens. Matter **32**, 043001 (2020).

[43] S. Hwan Chun, J.-W. Kim, J. Kim, H. Zheng, H. Zheng, C. C. Stoumpos, C. D. Malliakas, J. F. Mitchell, K. Mehlawat, Y. Singh, Y. Choi, T. Gog, A. Al-Zein, M. M. Sala, M. Krisch, J. Chaloupka, G. Jackeli, G. Khaliullin, and B. J. Kim, Direct evidence for dominant bond-directional interactions in a honeycomb lattice iridate Na2IrO3, Nat. Phys. **11**, 462 (2015).

[44] A. Revelli, M. Moretti Sala, G. Monaco, C. Hickey, P. Becker, F. Freund, A. Jesche, P. Gegenwart, T. Eschmann, F. L. Buessen, S. Trebst, P. H. M. van Loosdrecht, J. van den Brink, and M. Grüninger, Fingerprints of Kitaev physics in the magnetic excitations of honeycomb iridates, Phys. Rev. Res. **2**, 043094 (2020).

[45] J. Kim, J. Chaloupka, Y. Singh, J. W. Kim, B. J. Kim, D. Casa, A. Said, X. Huang, and T. Gog, Dynamic spin correlations in the honeycomb lattice Na_2IrO_3 measured by resonant inelastic x-ray scattering, Phys. Rev. X **10**, 021034 (2020).

[46] F. Forte, J. van den Brink, and M. Cuoco, Evolution of spinon Fermi surface and magnetic response of hyperkagome spin liquids, Phys. Rev. B **88**, 144422 (2013).

[47] R. R. P. Singh and J. Oitmaa, High-temperature series expansion study of the Heisenberg antiferromagnet on the hyperkagome lattice: Comparison with $Na_4Ir_3O_8$, Phys. Rev. B **85**, 104406 (2012).

[48] S. N. Gupta, P. V. Sriluckshmy, A. Balodhi, D. V. S. Muthu, S. R. Hassan, Y. Singh, T. V. Ramakrishnan, and A. K. Sood, Spin liquid like Raman signatures in the hyperkagome iridate $Na_4Ir_3O_8$, Phys. Rev. B **94**, 155153 (2016).

[49] S. Lee, B. H. Kim, M.-J. Seong, and K.-Y. Choi, Noncubic local distortions and spin-orbit excitons in K_2IrCl_6, Phys. Rev. B **105**, 184433 (2022).

[50] J.-H. Lee, Y. Choi, S.-H. Do, B. H. Kim, M.-J. Seong, and K.-Y. Choi, Multiple spin-orbit excitons in α-$RuCl_3$ from bulk to atomically thin layers, npj Quantum Mater. **6**, 43 (2021).

[51] S. K. Takahashi, J. Wang, A. Arsenault, T. Imai, M. Abramchuk, F. Tafti, and P. M. Singer, Spin excitations of a proximate Kitaev quantum spin liquid realized in Cu_2IrO_3, Phys. Rev. X **9**, 031047 (2019).

[52] Y. Shimizu, K. Miyagawa, K. Kanoda, M. Maesato, and G. Saito, Emergence of inhomogeneous moments from spin liquid in the triangular-lattice Mott insulator κ-$(ET)_2Cu_2(CN)_3$, Phys. Rev. B **73**, 140407(R) (2006).